

# Examination of Mars2020 shock-layer conditions via infrared emission spectroscopy of CO<sub>2</sub>

Augustin C. Tibere-Inglesse<sup>1</sup>

*NASA Postdoctoral Fellow at NASA Ames Research Center, Mountain View, CA, 94035, USA*

Thomas K. West IV<sup>2</sup>

*NASA Langley Research Center, Hampton, VA, 23681, USA*

Christopher C. Jelloian<sup>3</sup>, Nicolas Q. Minesi<sup>4</sup>, R. Mitchell Spearrin<sup>5</sup>

*University of California, Los Angeles (UCLA), Los Angeles, CA 90095, USA*

Justin Clarke<sup>6</sup>, Luca di Mare<sup>7</sup>, Matthew McGilvray<sup>8</sup>

*University of Oxford, England OX2 0ES, UK*

Brett A. Cruden<sup>9</sup>

*AMA Inc at NASA Ames Research Center, Mountain View, CA, 94035, USA*

A new test series was performed in the Electric Arc Shock Tube (EAST) facility, with the aim of reproducing flight conditions encountered during the Mars2020 mission entry into Mars atmosphere. For this test series, the EAST facility was instrumented with two spectrometers for Optical Emission Spectroscopy (OES) measurements and three mid-infrared lasers for Tunable Diode Laser Absorption Spectroscopy (TDLAS). This study focuses on the spectrally and spatially resolved radiance measured with OES. Comparison with CEA/NEQAIR and DPLR/NEQAIR simulations were made. For velocity above 2.7 km/s, measurements are found to lie between the different tested kinetic models, within  $\pm 10\%$ . Below 2.7 km/s, the chemistry appears to be frozen and measured radiance profiles are typically 10% above CEA

---

<sup>1</sup> Postdoctoral Fellow, Aerothermodynamics Branch

<sup>2</sup> Aerospace Engineer, Vehicle Analysis Branch, Systems Analysis and Concepts Directorate. Member AIAA

<sup>3</sup> Ph.D. Student, Mechanical and Aerospace Engineering Department, Member AIAA.

<sup>4</sup> Postdoctoral Researcher, Mechanical and Aerospace Engineering Department, Member AIAA.

<sup>5</sup> Assistant Professor, Mechanical and Aerospace Engineering Department, Member AIAA.

<sup>6</sup> Ph.D. Student, Oxford Thermofluids Institute, Department of Engineering Science.

<sup>7</sup> Associate Professor, Oxford Thermofluids Institute, Department of Engineering Science.

<sup>8</sup> Associate Professor, Oxford Thermofluids Institute, Department of Engineering, Member AIAA

<sup>9</sup> Senior Research Scientist, Aerothermodynamics Branch, and Associate Fellow AIAA.

predictions. This difference is explained by shock deceleration effects. Finally, comparison between OES and TDLAS data are made and show a good agreement on the measured temperature and  $\text{CO}_2$  number density profiles using the two diagnostics, typically within 10 and 5%, respectively.

## I. Introduction

On February 18, 2021, the NASA Mars 2020 mission successfully landed the Perseverance rover onto the surface of Mars. During entry into the Martian atmosphere, the Mars Entry, Descent, and Landing Instrumentation 2 (MEDLI2) sensor suite collected in-flight pressure, temperature, and heat flux data on the aeroshell [1] [2]. Of particular relevance to this work, MEDLI2 included two total heat flux sensors and one radiometer to directly measure the convective and radiative heating on the afterbody. A comparison between the total measured and predicted radiative heat flux – using two different kinetic models, referred to as “Cruden” [3] and “Johnston” [4] – at the sensor MTB08 location is presented in Figure 1. The difference between the measurements and the prediction represents the convective heat flux component of the measured total heat flux. The Cruden mechanism gives a better agreement early in the heat pulse while later on, a better agreement is observed with the Johnston mechanism predictions. Comparison between predicted and measured radiative fluxes were also made using the MTB08 sensor and showed disagreement increasing up to 50% with entry pulse time, which can be attributed to blockage by ablation products [5]. Previous measurements were also performed during the Schiaparelli capsule entry and showed good agreement (within 16%) between measured and computed back shell heating but the complete dataset was not recovered due to the failed landing of Schiaparelli [6].

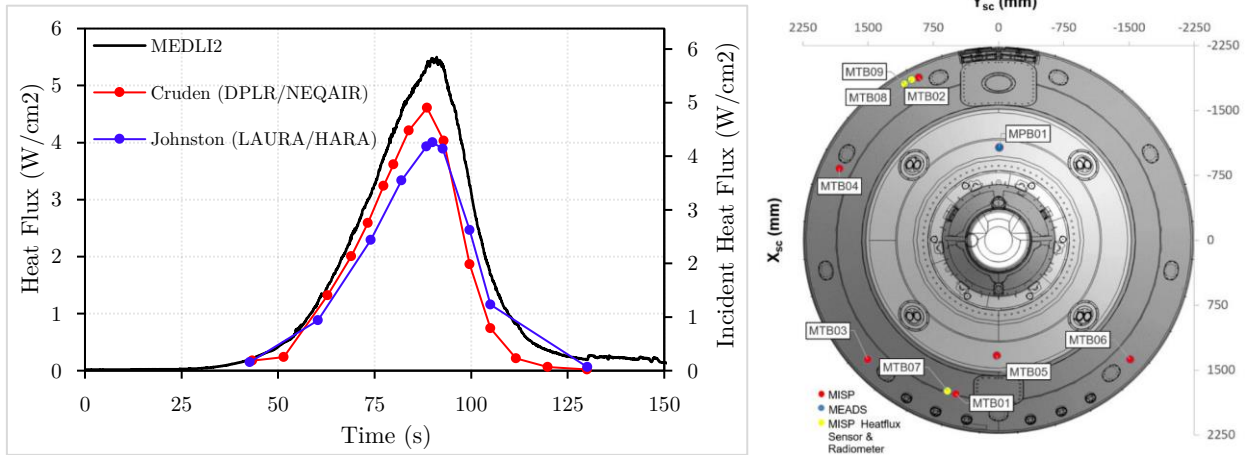


Figure 1: Left: Comparison between the flight data total heat flux measurements with the MTB08 sensor and the radiative heat flux prediction using the Cruden [3] or Johnston [4] kinetic model. Right: Location of the sensor in the Mars2020 backshell [2].

Reproduction of flight conditions in ground test facilities is of interest for establishing ground-to-flight traceability and may provide additional data that allows for validation of predictive models. Such a test was previously conducted in the Electric Arc Shock Tube (EAST) facility at NASA Ames Research Center for the Mars Science Laboratory and was able to reconcile most of the discrepancy in stagnation line heating measured by the original MEDLI sensors [7]. However, no similar test has been performed that is relevant to heating on the afterbody of the Mars2020 mission but is motivated by the difference in the predictions observed in Figure 1. It has recently been shown that the radiation on the afterbody of a capsule could be

modeled by radiation of an oblique shock. [8] This shock tube informed bias method states that, in particle time, the normal component velocity of an oblique shock has similarity with an incident shock. This similarity is used here to find shock tube conditions that are relevant to the Mars2020 backshell. Fifty-nine (59) shots were performed during this test series with velocities varying from 1.17 to 3.75 km/s and fill pressure (mostly) between 1.1 and 2.0 Torr. A summary of most of the shots performed is given in Figure 2. The pressures of 1.1, 1.5 and 2 Torr roughly corresponds to a flight time of 92, 101 and 144 s, respectively. These conditions were chosen to represent peak heating, half of the peak and closeout of the radiation pulse, as seen on Figure 1. Measurements of lower pressure conditions, corresponding to the rising portion of the heat pulse, will be conducted in a future test series using the EAST facility 53 cm Low Density Shock Tube, currently being installed. This paper will present the results and analysis of the Optical Emission Spectroscopy (OES) measurements made during this test series. A companion paper [9] describes tunable diode laser absorption spectroscopy (TDLAS) performed during the same test.

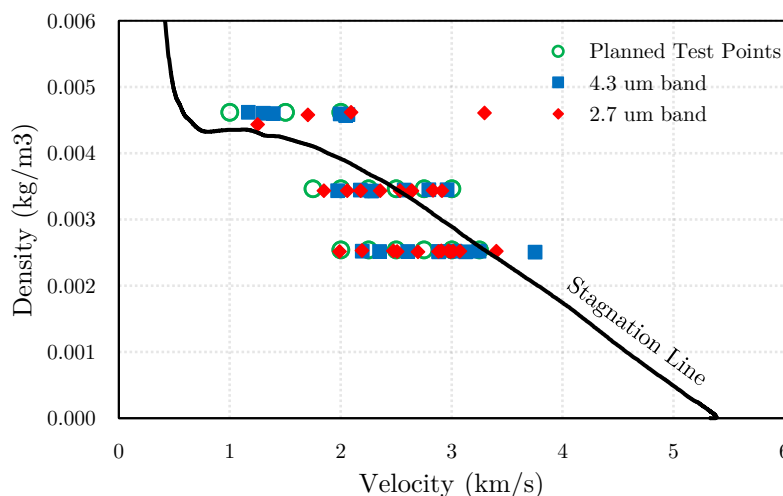


Figure 2: Summary of most of the shots performed, with the two different infrared spectrometer settings (see section II). The conditions chosen according to the shock tube informed bias methodology (circle) and the stagnation line trajectory (line) are also shown for comparison.

## II. Experimental setup

The Electric Arc Shock Tube (EAST) facility has been described in detail in previous publications [10] [11]. This facility is composed of a 1.2 MJ, 40 kV capacitor bank that drives a 10.16 cm aluminum shock tube. The test gas consists of simulated Mars atmosphere – 95.4%  $\text{CO}_2$ , 2.6%  $\text{N}_2$ , 2.0% Ar. A schematic of the EAST facility is presented in Figure 3. The test section of the facility is usually instrumented with four spectrometers looking at different wavelength regions: one in the Vacuum Ultraviolet, one in the UV/visible, one in the visible/near-infrared and one in the mid infrared [10], see Figure 4. However, based on the previous test series at similar conditions [7], no significant radiation is expected to be measured except in the infrared region. The measurements in this test therefore included data from only two cameras, looking at UV/visible and infrared emission, respectively. The radiation in the UV/visible consisted of weak continuum radiation and is not analyzed in this paper. Only the data from the IR camera will be presented. Two different settings for the infrared spectrometer were studied to measure the 4.2  $\mu\text{m}$  fundamental and 2.7  $\mu\text{m}$  overtone bands of  $\text{CO}_2$  which are the main source of radiation in Mars entry. Tunable Diode Laser

Absorption Spectroscopy (TDLAS) was also implemented for this test series and results are presented in a companion paper [9]. A summary of all shots performed with useable emission data is given in Table 1.

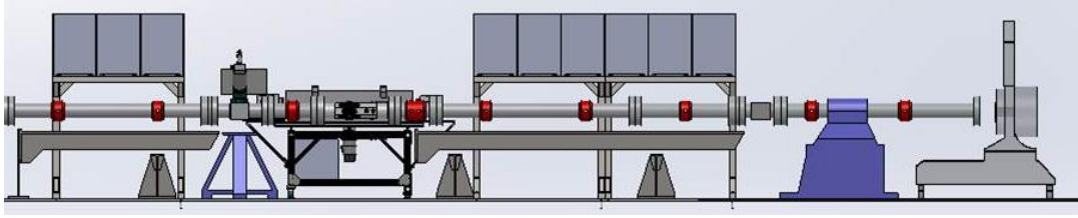


Figure 3: Schematic of the EAST facility.

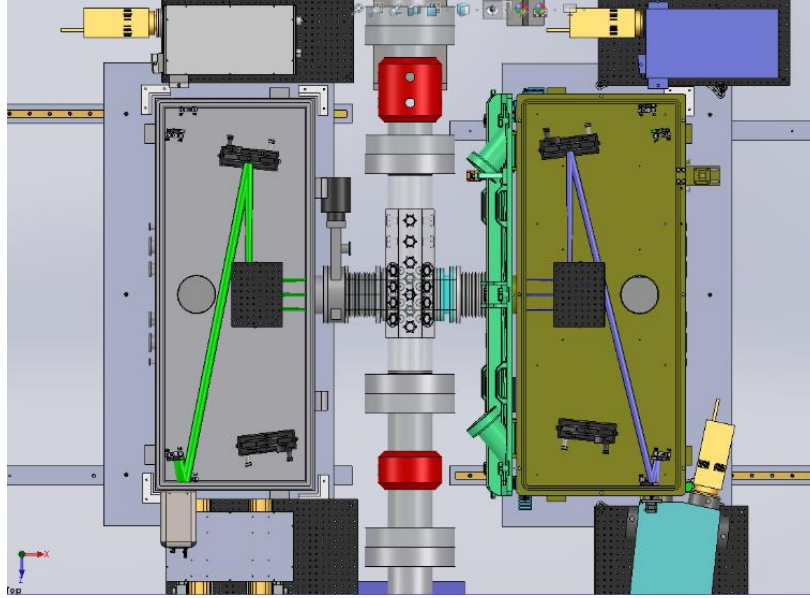


Figure 4: Instrumentation setup of the test section for OES.

Table 1: Summary of all shots performed with useable data. The spectrometer settings are changed to measure both 4.2 and 2.7  $\mu\text{m}$   $\text{CO}_2$  bands.

Shot number	Velocity (km/s)	Fill pressure (Torr)	$\text{CO}_2$ band measured ( $\mu\text{m}$ )
2	3.25	1.1	4.2
3	3.03	1.1	4.2
4	2.60	1.1	4.2
6	2.35	1.1	4.2
7	2.19	1.1	4.2
8	2.88	1.1	4.2
9	3.40	1.1	2.7
10	3.07	1.1	2.7
11	2.51	1.1	2.7
12	2.94	1.1	2.7
16	1.99	1.1	2.7
17	2.19	1.1	2.7
18	3.01	1.1	2.7
19	2.88	1.1	2.7

20	2.70	1.1	2.7
21	2.96	1.5	4.2
22	2.79	1.5	4.2
23	2.57	1.5	4.2
24	2.17	1.5	4.2
25	1.97	1.5	4.2
26	2.28	1.5	4.2
27	2.91	1.5	2.7
28	2.64	1.5	2.7
29	2.53	1.5	2.7
30	2.18	1.5	2.7
31	2.06	1.5	2.7
32	2.64	1.5	2.7
33	2.83	1.5	2.7
34	1.85	1.5	2.7
35	2.35	1.5	2.7
36	2.00	2.0	4.2
39	1.39	2.0	4.2
40	1.30	2.0	4.2
42	1.70	2.0	2.7
46	1.96	0.5	4.2
52	3.75	1.1	4.2
54	2.49	8.8	4.2
55	1.25	1.9	4.2
57	1.94	1.9	4.2
58	1.17	2.0	4.2
59	2.68	8.8	4.2

### III. Approach

An example of experimental data obtained from test 64 campaign is presented in Figure 5. The data are spectrally and spatially resolved, giving a 3D map of radiance versus these two variables. Horizontal and vertical slices shown in Figure 5 represent the integrated radiance versus the spectral and the spatial variable, respectively. Two measurements are shown, corresponding to the two CO<sub>2</sub> bands measured in this campaign. The vertical slices are used to get an estimate of the shock front location. The shock front location may differ from shot to shot.

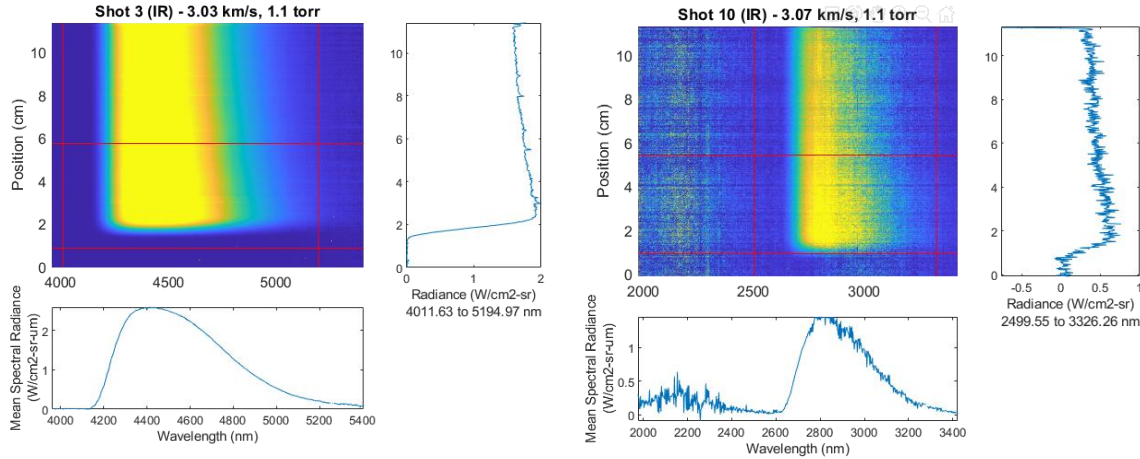


Figure 5: 3D spectral intensity maps obtained for shot 3 and 10 with the IR camera

In this work, both the spectral radiance and the total radiance are compared with computational predictions. Comparisons of spectrally resolved data consist of the radiance binned over 1 cm, starting 2 cm after the shock front. This spectrum is then compared with NEQAIR [12] predictions, based on equilibrium (chemical and thermal) and frozen conditions computed using CEA [13] [14]. Comparison of the spatial variation is based on the radiance integrated over 4100-5400 nm or 2600-2800 nm depending on the spectrometer setting and band being measured. The 4100-5400 nm range allows comparison to radiation from the fundamental 4.2  $\mu\text{m}$  band of  $\text{CO}_2$ . At lower velocities, below 2 km/s, the wavelength range is reduced to 4100-4800 nm to prevent integrating noise signal. The 2600-2800 nm range is used for comparison of the 2.7  $\mu\text{m}$  band. Even though this band was measured out to 3400 nm, the higher wavelength range was not used due to a poor signal to noise ratio above 2800 nm. Measurements below 2400 nm suffer from ambient absorption and are too noisy to discern signal, although some radiation is predicted to occur in this region. The measured radiance profiles are binned over  $\pm 2$  cm around the shock front – which was previously defined as the nonequilibrium radiance metric [15, 16], but will be referred as the peak radiance in this paper – and compared with CEA and CFD predictions. CFD simulations were performed using DPLR [17] by extracting the stagnation line from a flow around a 1-m sphere simulation, at the freestream conditions equal to the test gas temperature and pressure, and the measured velocity, in a similar way than in Refs [3, 18]. Three different kinetic models were used and are denoted as Park [19], Johnston [4] and Cruden [3], with the latter being updated to use the recent  $\text{O}_2$  dissociation kinetic rate reported by Streicher *et al* [20]. These models were previously tested mainly for velocities above 3 km/s, and this work may extend their validation range to lower velocity.

#### IV. Optical Emission Spectroscopy results

Typical comparison of integrated radiance profiles and spectra between measurements and simulations are presented in Figure 6-9 for high to low velocities at fill pressures of 1.1 and 1.5 Torr. For higher velocities ( $>2.7$  km/s), the integrated radiance profile increases at the shock front then decreases towards its equilibrium value, as is expected in a reacting flow. At 1.1 Torr, the radiance peaks below the frozen value, while the frozen limit is obtained at 1.5 Torr. The measured radiance profile is generally between the Johnston/Park and Cruden model predictions at 1.1 Torr and is closer to Cruden mechanisms at 1.5 Torr. For velocities below 2.6 km/s, the chemistry in the shock appears to be frozen in the time scale of the experiment, with a value up to 10% higher than the frozen condition predicted by CEA. Examination of



the spectra shows that this higher value is observed at every wavelength. Since the chemistry is frozen for these lower velocity cases, all DPLR models gave similar results.

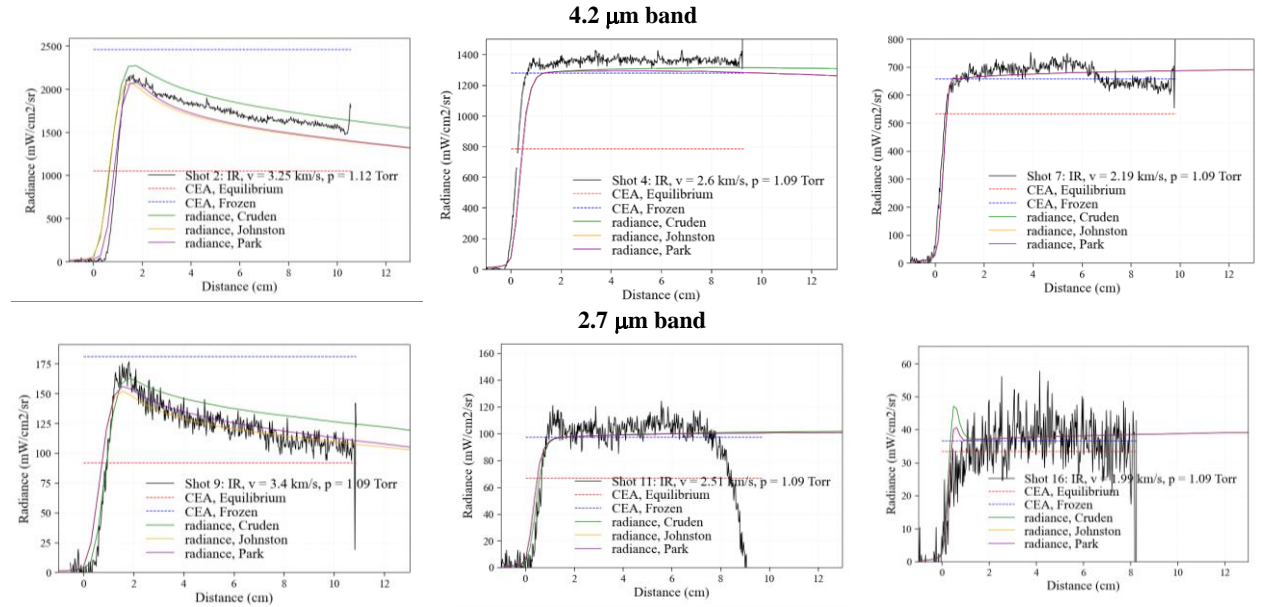


Figure 6: Comparison between measured (black) and computed integrated radiance profiles using CEA/NEQAIR or DPLR/NEQAIR predictions for different shots at 1.1 Torr. Top: for the 4.2  $\mu\text{m}$  band. Bottom: for the 2.7  $\mu\text{m}$  band

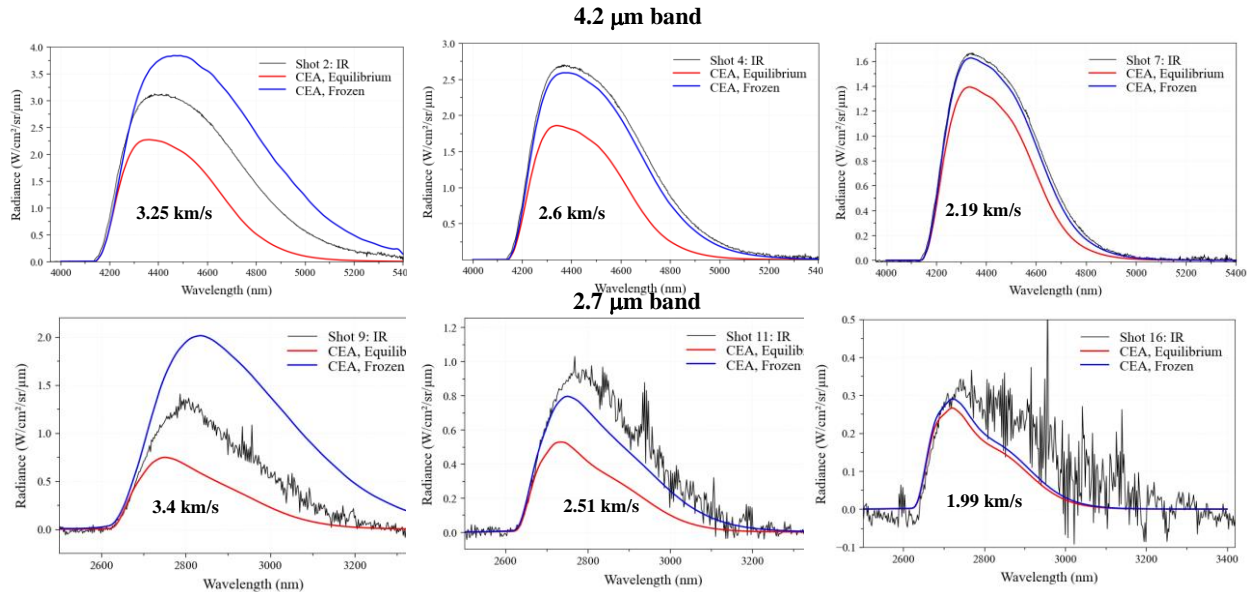


Figure 7: Comparison between measured spectra integrated over 1 cm starting around 2 cm from the shock front and CEA/NEQAIR predictions for different shots at 1.1 Torr

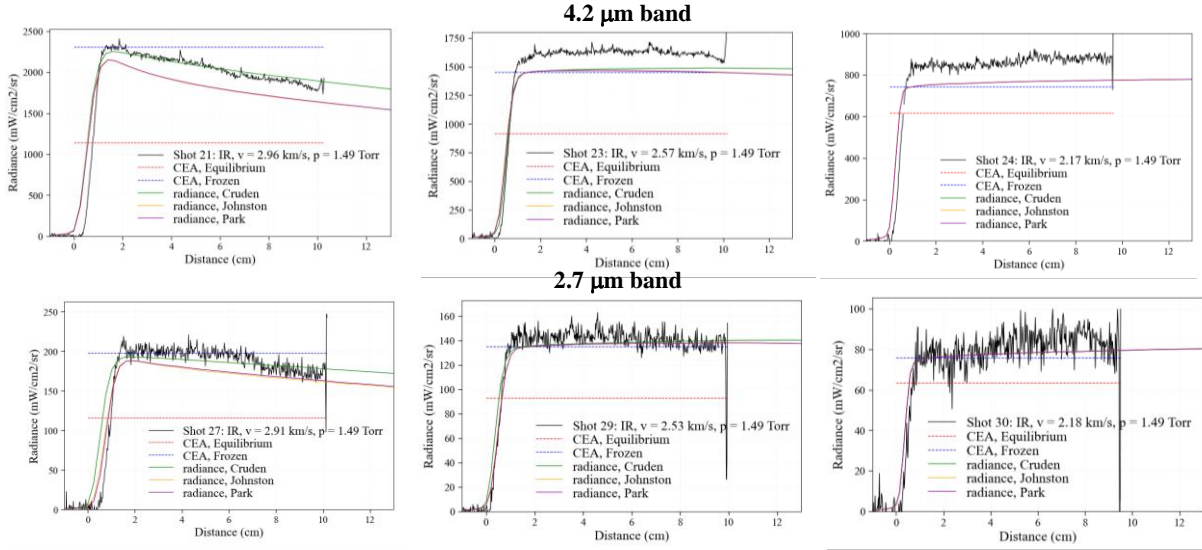


Figure 8: Comparison between measured (black) and computed integrated radiance profiles using CEA/NEQAIR or DPLR/NEQAIR predictions for different shots at 1.5 Torr. Top: for the 4.2  $\mu\text{m}$  band. Bottom: for the 2.7  $\mu\text{m}$ .

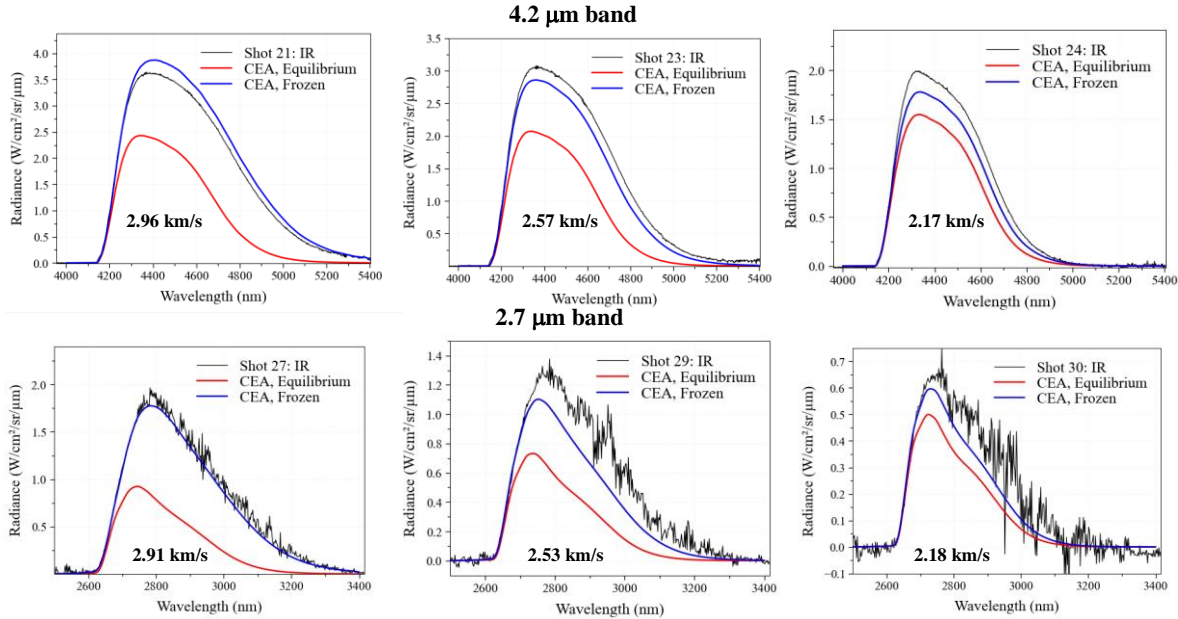


Figure 9: Comparison between measured spectra integrated over 1 cm starting around 2 cm from the shock front and CEA/NEQAIR predictions for different shots at 1.5 Torr

To compare the results from all shots performed during the test series, the peak radiance at fill pressures of 1.1, 1.5 and 2.0 torr for both  $\text{CO}_2$  bands are presented in Figure 10. The error bars are based on the noise level measured on the radiance profile (as seen in figs. 6 and 8) around a moving average value. At velocities below 2.7 km/s, the measured peak radiance is underpredicted by around 10% for both bands and every fill pressure. Each model gives similar results as they predict a quick rise to the frozen radiance value – see Figures 6 and 8. Reasons for this discrepancy will be the focus of Section V. At 1.1 torr and below 2.3 km/s,



a relatively good agreement with frozen conditions is observed. For velocities above 2.7 km/s, the measured radiance lies between the Cruden and Johnston model. For 3.75 km/s, the highest velocity reported in this paper, a good agreement is observed between the measurement and the Cruden model. This is consistent with the results from a previous test series reported in Ref. [21] which showed a better agreement between measurements and predictions using the Cruden model from velocity from 3.8 to 6.6 km/s.

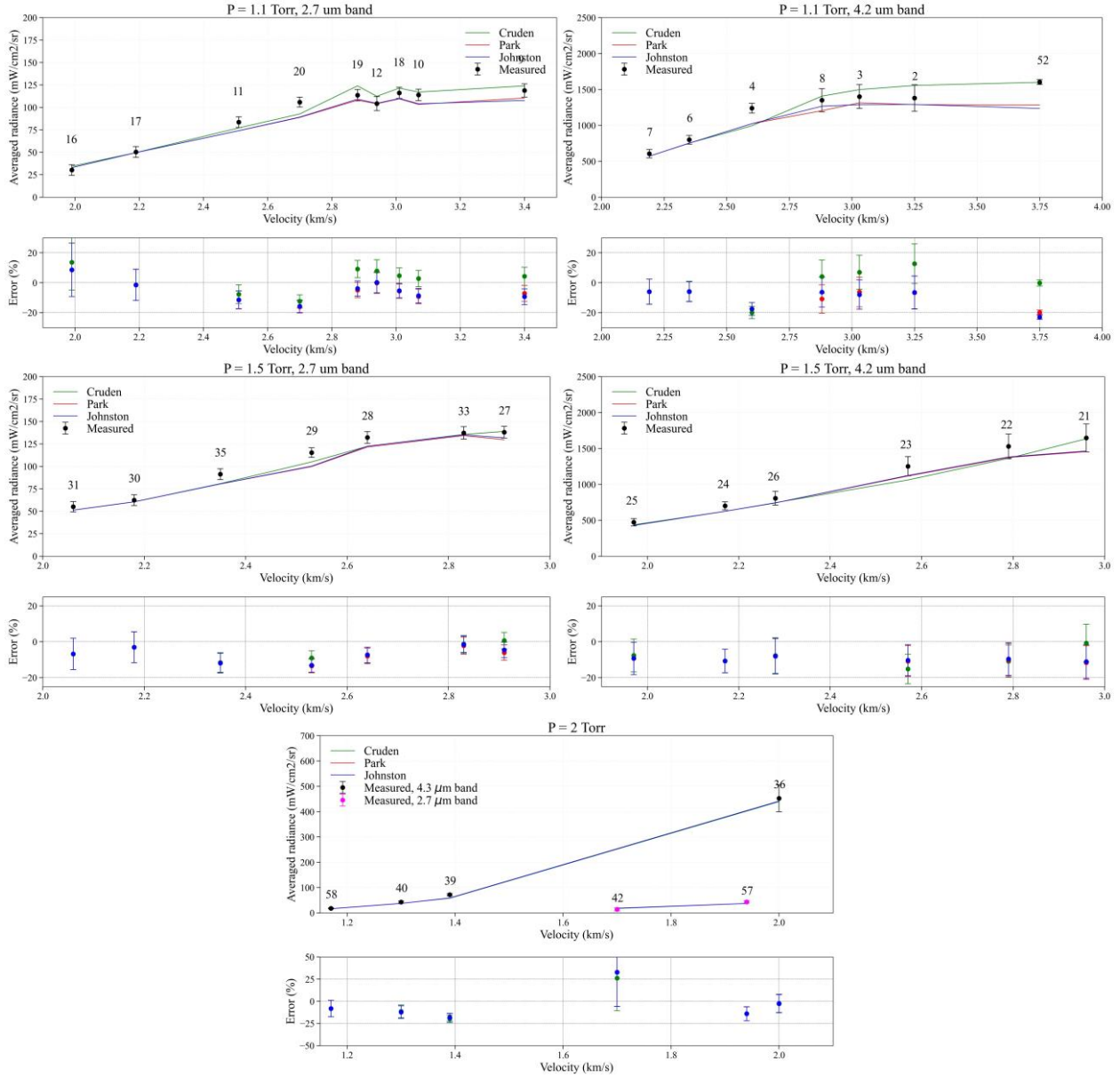


Figure 10: Comparison between measured and computed peak radiance ( $\pm 2$  cm from the shock front) for all fill pressure and both  $\text{CO}_2$  bands

One of the primary goals of this test series is to validate the models used for radiative heating in the backshell using the shock tube informed bias and flowfield property binning methods [22, 5]. For a given point in the backshell, this method estimates where the gas emitting the radiation impacting the backshell originates from, which is then related to both normal shock velocity and particle time. This analysis was

performed here for the Mars2020 entry trajectory at the locations corresponding to the heat flux and radiometer gauges shown in Figure 11. Two locations are presented on the lee and wind side. Figure 11 also shows the radiative heating bin distributions for a freestream pressure of 1.1 and 1.5 Torr. For the 1.1 Torr condition, most of the radiation measured during the entry is predicted to come from a shocked gas at 3 to 3.2 km/s, after travelling 1 to 8 ms from the shock front (in particle time) at the MBT08 location, and from 2.7 to 3 km/s, after travelling from 1 to 7 ms, at the MTB07 location. At 1.5 Torr, the relevant velocities are from 2.5 to 2.6 km/s and from 2.4 to 2.5 km/s and particle time has increased to be mostly between 3 to 12 ms and 2 to 10 ms, at the MTB08 and MTB07 location, respectively. Considering the case at 1.5 Torr and 2.5 km/s, the particle velocity behind the shock front is expected to be 230 m/s based on CEA calculations. The experiments only allowed measured radiation up to 10 cm from the shock front, i.e. a particle time around 400  $\mu$ s. This value is typical of the maximum particle time for most shots. These times are lower than those indicated in Figure 11, which suggests they may be more relevant for positions closer on the backshell or at lower pressure where binary scaling can be applied [8]. Nevertheless, the measurements do give information about chemical relaxation rates and can be used to test the applicability of different reaction models at these conditions.

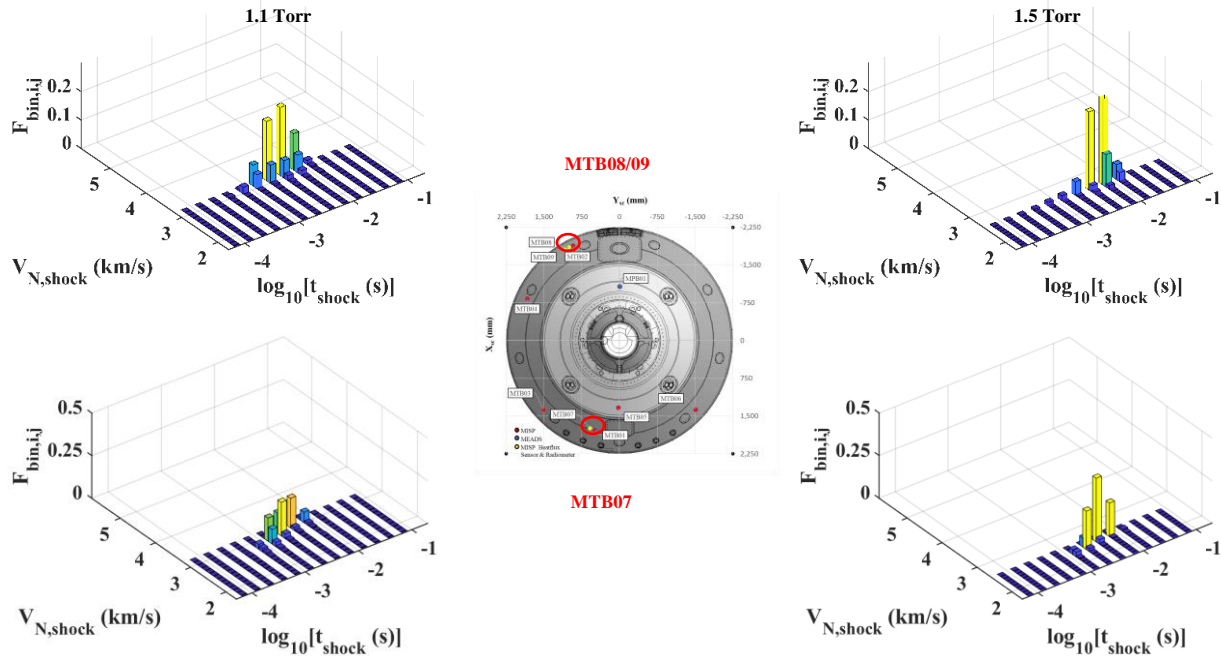


Figure 11: Radiative heating bin distributions for the surface point MTB07 (bottom) and MTB08/MTB09 (top) for the Mars2020 entry at a freestream pressure of 1.1 (left) and 1.5 Torr (right). The locations of the sensors are shown in the center.

While the full particle time desired was not achieved, the evolution of the error predictions further away from the shock are analyzed as an indicator of the model accuracy. As an example, Figure 12 shows the same comparison made in Figure 10, but for an averaged radiance integrated over 0.25-0.35 ms particle time, which corresponds to the largest particle time available for every shot. To calculate the particle time, the velocity behind the shock wave is taken from CFD results ( $u_{CFD}$ ) and used to convert the distance behind the shock front ( $d_{measured}$ ) to time, i.e.  $t_{part} = d_{measured}/u_{CFD}$ . Frozen and equilibrium radiance values

are shown for comparison. All models predict frozen chemistry for velocities below 2.7 km/s for all pressures, as discussed previously. As before, the measured radiance is up to 10% higher than the frozen value. This behavior is discussed in Section V. Above 2.7 km/s, the measured radiance diverges from the frozen value toward the equilibrium value, as expected. At 1.1 Torr, the 2.7  $\mu\text{m}$  band radiation agrees well with the Johnston/Park models, while it lies between the models for the 4.2  $\mu\text{m}$  bands, with a relative error around  $\pm 10\%$ . Between 2.8 and 3.2 km/s, the radiance prediction of the 2.7  $\mu\text{m}$  error is consistently higher by about 5% than the prediction error of the 4.2  $\mu\text{m}$  band. This was previously observed in Ref. [7] with larger discrepancies. At larger velocity, 3.75 km/s, all models diverge from the measurements and predict a faster relaxation to equilibrium than measured. At 1.5 Torr, a better agreement (within 5%) is observed with the Cruden model, while the other two underpredict the measured radiation by about 10%.

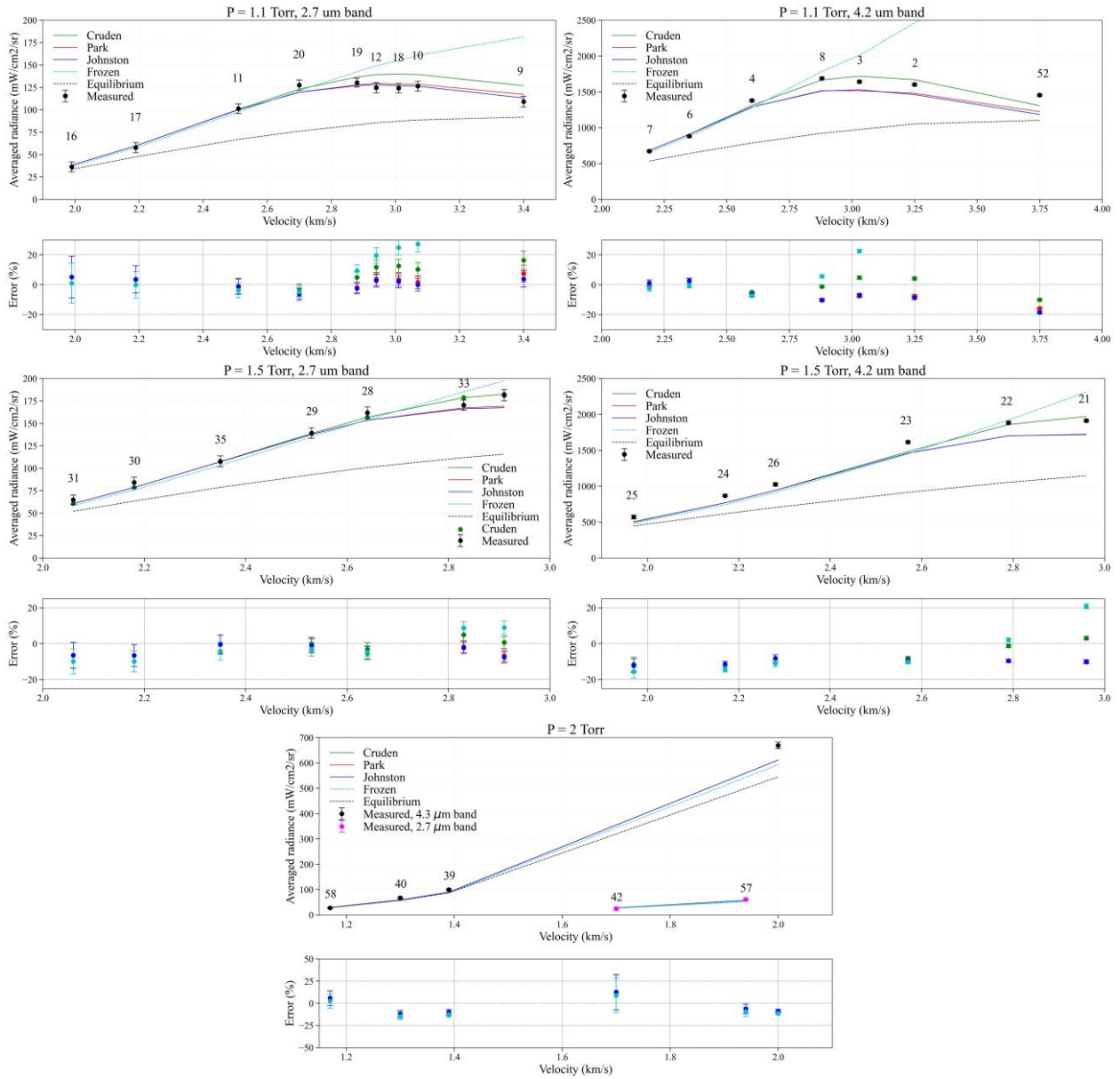


Figure 12: Comparison between measured and computed averaged radiance (over 250 to 350  $\mu\text{s}$  in particle time) for all fill pressure and both  $\text{CO}_2$  bands

As the chemistry appears frozen below 2.7 km/s, the higher velocity tests are the only ones able to differentiate reaction rate models. Based on Figure 11, these high velocity tests are also the most important as they contribute more to the backshell radiative heating at this location. To assess the total uncertainties on the backshell, the evolution of the prediction error with particle time for the highest velocity shots performed in this test series are given in Figure 13 for a fill pressure of 1.1 and 1.5 Torr and velocities around 3.3 and 2.9 km/s, respectively. Both CO<sub>2</sub> bands are considered, and a total estimated error is given, which is computed using the relative intensity of both bands:

$$\varepsilon_{tot} = \frac{\varepsilon_{2.7\mu m} \Gamma_{2.7\mu m} + \varepsilon_{4.3\mu m} \Gamma_{4.3\mu m}}{\Gamma_{2.7\mu m} + \Gamma_{4.3\mu m}}$$

where  $\Gamma$  represents the cumulative radiance of a given band.

At 1.1 Torr, the error in the Cruden model is around 7% at all positions behind the shock while the Park/Johnston models start with a +2% error that decreases steadily to -10% at 300  $\mu$ s. At 1.5 Torr, the error for the Park/Johnston model starts around -5% and decreases to around -10% after 100  $\mu$ s and later, while the error with the Cruden model starts at around -10% and then agrees well (within  $\pm 2\%$ ) with the experiments after 100  $\mu$ s. To estimate the error in the model at the Mars2020 radiometer location, these profiles need to be extrapolated to values from 1-10 ms.

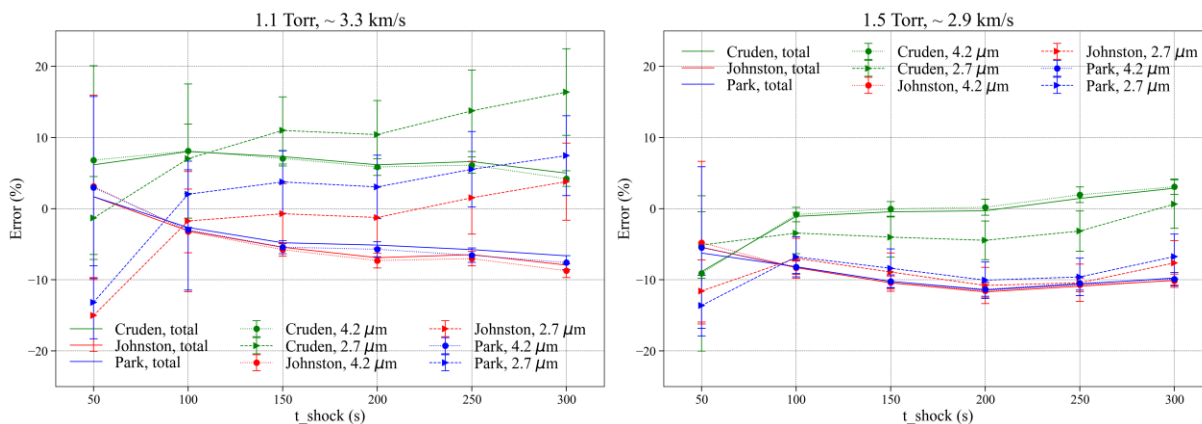


Figure 13: Evolution of the error between predicted and measured radiance as a function of particle time, for the three models considered.

Another quantity to consider is the relaxation time to equilibrium, after which models and experiments should predict the same radiance value. The characteristic relaxation time to equilibrium was obtained by fitting the radiance profiles with an exponential curve trending to the equilibrium value obtained by CEA. Both measured and predicted profiles were fit the same way to ensure consistency in the comparison. Despite some scatter in the data, the curves show relative consistency as a function of velocity, with the characteristic relaxation time decreasing as the velocity increases. Comparison between shots at the same velocity for the two different pressures also show similar values, which might be expected for a relatively small change in pressure. The measured relaxation time obtained by fitting the 4.2  $\mu$ m band shows a good agreement with the Cruden mechanism, while the Park/Johnston model seems to underpredict it by up to 40%. For the 2.7  $\mu$ m band, the predicted relaxation time using the Cruden mechanism overpredicts the measurements by about 30%, while the Park/Johnston model generally show a better agreement. The predicted relaxation time using the 2.7  $\mu$ m band is consistently higher than that predicted for the 4.2  $\mu$ m band, which is the opposite of the experimental observation. These differences are believed to be related to

shock deceleration. The  $4.2\ \mu\text{m}$  band, being optically thick [7], should be more indicative of the post-shock temperature while the  $2.7\ \mu\text{m}$  band should scale with  $\text{CO}_2$  number density. As will be shown in Sect. V, the shock deceleration shows a greater impact on  $\text{CO}_2$  number density than temperature. Thus, the apparent agreement with the Johnston model for this band may also be an artifact of shock deceleration. For the range of data studied, the relaxation time is between 0.5 to 2 ms.

For the 1.5 Torr case, most of the radiation measured by the MTB08/09 sensors originates from shock velocities between 2.5 to 2.6 km/s, and between 2.4 and 2.5 km/s at the MTB07 location. In the timescale of our experiments, the chemistry appears to be frozen in these conditions, so tests cannot be used to infer the prediction accuracy at the flight timescale. A shot at 2.5 km/s, 9 Torr was performed which, based on the test time and binary scaling would provide an equivalent particle time of about 1 ms at 1.5 Torr, which is still shorter than the flight timescale. This test was also found to be frozen in the experimental measurement and by the Cruden model, though Park and Johnston models predicted some reaction in this timescale. However, since the flight timescale is not matched, no conclusions about the accuracy of the flight predictions are made at this time.

For the 1.1 Torr case, the relaxation times are about 3x less than the particle time from which the gas radiation originates from. Figure 13 indicates the radiation might be underpredicted by up to 10% with the Park/Johnston models, and overpredicted by up to 7% for the Cruden model. To estimate the error at flight scale, the exponential curve fits used to obtain relaxation time are extended out to 8 ms to be representative of the radiance measured at the MTB07 location. The error between the fitted predicted radiance curve and the measurements show an overestimation of 2% using the Cruden mechanism, and a 3% underestimation using the Johnston mechanism. This is consistent with the difference between the radiance predicted by the two models in Figure 1 at 92 s (about 5%). At the MTB07 location, the velocity range of interest is 2.7 km/s to 3 km/s. Using the same procedure using shots around 2.9 km/s, the total error between the measured and predicted radiance at the MTB07 location would be  $-6.5\%$  and  $+2\%$  with the Johnston and Cruden model, respectively. This is also consistent with the difference the radiance predicted by the two models at the MTB07 location (about 10%). The relative consistency in the disagreement between the two models from this method and the corresponding full vehicle predictions at both vehicle locations serves to validate the shock tube informed bias methodology.

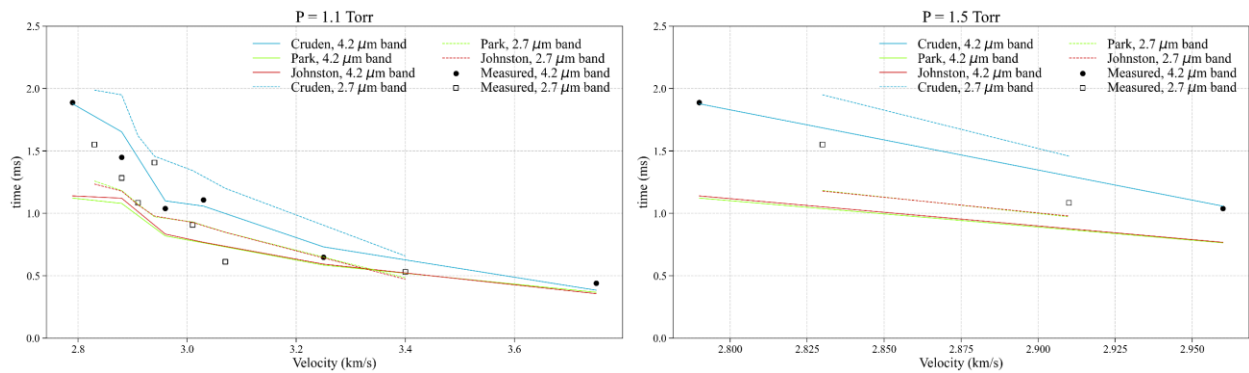


Figure 14: Estimated relaxation time to equilibrium based on the predicted (lines) and measured (points) radiance profiles for all shots above 2.7 km/s, for both  $\text{CO}_2$  bands considered

## V. Effect of shock deceleration on the measured radiance

It has previously been proposed that radiation in EAST is affected by the deceleration of the shock wave as it traverses the tube [23]. This was experimentally verified by varying the shock history between accelerating and decelerating profiles for the same final shock speed in the Oxford T6 facility for air radiance [24, 25] showed the test slug had significant flow non-uniformities caused by the decelerating/accelerating shock profiles down the tube and boundary layer effects. From this work, the LASTA code [26] was developed to predict the influence of the shock deceleration on measurements made downstream in the shock tube. The methodology underpinning LASTA is the assumption that the shock trajectory fully captures the complex wave processes present in a shock tube during a test. Therefore, for a given shock speed profile with a specified fill condition, the solver can reproduce the pressure and temperature variations present as a consequence of changes in shock speed. The gas can be assumed to have ideal, equilibrium, or frozen chemistry. The LASTA solver uses a quasi-one-dimensional, Lagrangian formulation in which uniformly distributed discrete gas slices are placed along the tube. As the shock propagates down the tube, the slices are activated and processed by the shock at the appropriate shock speed according to the specified trajectory. After this, forward and backward travelling waves (in the shock frame of reference) evolve the condition of the activated slices. The rearward-travelling waves are caused by changing post-shock conditions; the forward-travelling waves are comprised of driver pressure fluctuations, waves due to mass loss to the boundary layer, and waves caused by mixing and reflections at the contact surface. By tracking the waves as they traverse the test slug, their influence on each gas slice can be determined. The LASTA approach accurately reproduces the experimental test slug, while taking a fraction of the time of a full axisymmetric simulation of the experiment. The LASTA code has recently been used to explain discrepancies discussed in older EAST data. [27] The code is employed in this work to examine the effects of shock deceleration and wave propagation on the measured radiance. LASTA simulations were performed using the measured shock position versus time history obtained from the EAST pressure sensors. The LASTA outputs were then used as input to NEQAIR to obtain a radiance profile.

Several shots were selected for comparison, including the full range of fill pressures and a case where the measured and frozen radiance appeared to agree despite a non-uniform velocity profile. A comparison between the measured and predicted radiance profiles is presented in Figure 15. In all cases, a good agreement between the LASTA predictions and measurements are observed and can explain the discrepancies of up to 15% which were observed in section IV. For shots 23 and 29, the shock velocity at the test section location is similar, but the measured radiance profiles show differing agreement to the frozen solution (<3% discrepancy vs. 10% higher). In this case LASTA has correctly predicted the radiance of both shocks, due mostly to differences in how the position versus time (and hence velocity) curve is interpolated. (Note that the velocity interpolation is performed independently of the radiation calculation, so is not adjusted to match.) The increasing radiance with position, however, may be attributed deceleration of the shock wave and is reproduced within experimental accuracy by the LASTA code. This demonstrates that the differences observed in Figure 12 between measured and frozen radiance below 2.7 km/s are likely a result of the velocity determination and, to a lesser extent, shock deceleration. A good agreement between frozen and measured radiance is obtained with the Lagrangian approach.



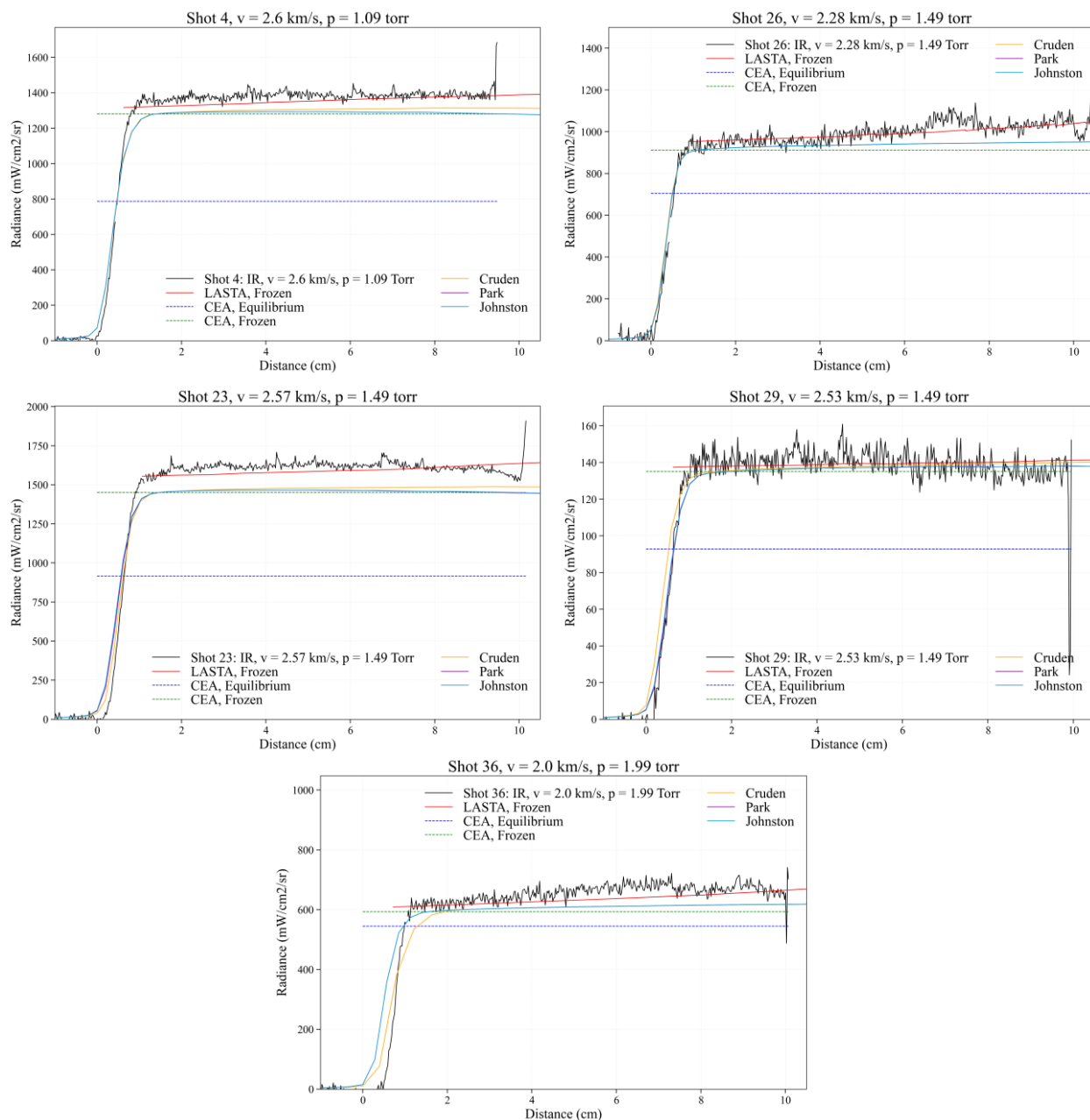


Figure 15: Comparison between measured and predicted radiance profiles for shots with frozen chemistry where LASTA simulations were performed.

The impact of shock deceleration on the equilibrium radiance was examined for the fastest shot of this test series, 3.75 km/s at 1.1 Torr. Based on Figure 12, the CFD simulations predict the flow to be closer to equilibrium conditions than what was measured. The radiance is predicted to be 7, 10 and 16% higher than the equilibrium radiance 300  $\mu$ s from the shock front with the Johnston, Park and Cruden mechanisms, respectively while the measured radiance is 25% higher. LASTA simulations for equilibrium conditions are shown in Figure 16. The equilibrium radiance computed by LASTA increases behind the shock front due to shock deceleration. Comparing the measured and LASTA equilibrium radiance 300  $\mu$ s/8 cm from the

shock front yield a difference of 18%, which is similar to the difference from equilibrium predicted by the Cruden mechanism. The result suggests that including the impact of shock deceleration on the Cruden curve would cause it to more closely follow the experimental measurement.

While simply adding the offset due to deceleration predicted by LASTA may reconcile the model, a better comparison would consider a reacting flow in the presence of deceleration. To provide an approximation of this effect, the LASTA simulations were used to obtain the shock velocity and enthalpy from which the gas at a given position behind the shock front originates. For each of these solutions, a 0D kinetic simulation is then performed with the Cantera code [28] over the time of flight returned by LASTA. In this case, the time of flight is a combination of boundary layer effects changing the axial velocity and to a lesser extent, shock speed variation down the tube [29, 30, 26]. Performing this calculation at different locations behind the shock then obtains a gas temperature and number density versus distance behind the shock. NEQAIR simulations are then performed with these inputs to get radiance profiles. Results using the Cruden mechanism are presented in Figure 16 along with the corresponding DPLR stagnation line solutions already discussed. The corresponding frozen radiation profile from LASTA is also shown for comparison. Even though the frozen radiance is impacted by the shock deceleration, the 0D reactor simulation produces very similar results to the DPLR stagnation line profile. Therefore, the comparison between the model predictions and the experiments performed in section IV is still supported. Overall, these comparisons show the importance of taking into account shock deceleration while analyzing shock tube data.

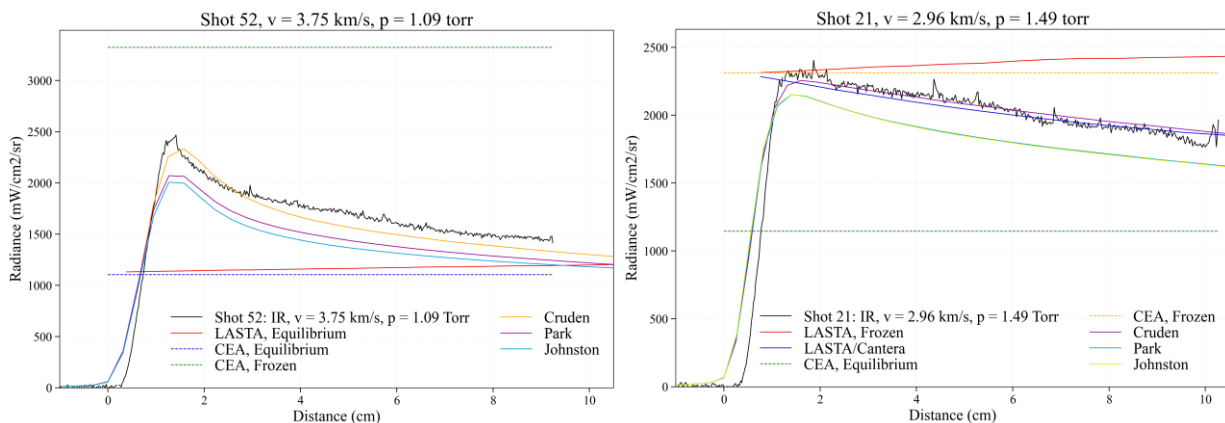


Figure 16: Comparison between measured and predicted radiance profiles including LASTA simulations, for an equilibrium (left) and reacting case (right).

## VI. Comparison with TDLAS measurements

Finally, the data obtained from OES were compared with the TDLAS measurements performed and presented in a companion paper [9]. In order to compare the temporally resolved TDLAS data with OES measurements, the measured radiance was binned over 0.5/1 cm intervals and fit to obtain post-shock number densities and temperatures. The binning interval is chosen as a compromise between having both good signal-to-noise ratio and spatial resolution. The fits are performed using the NEQAIR radiation code in a similar way as presented in Refs [26] [27]. Reported uncertainties in the emission data only represent the error from the fitting parameters and do not take into account any other sources of uncertainties such as those coming from the radiation model. LAS uncertainties consider the fit as well as the underlying

linestrength model uncertainties. The temperature and  $\text{CO}_2$  number density profiles obtained by OES and TDLAS measurements are compared in Figure 17 with CFD and LASTA predictions.

Temperature results from the emission and absorption techniques often showed a disagreement with LAS being 5 – 10% below temperature measured from OES across the range of shock velocities. A few examples are shown in Figure 17. For the reacting case (shot 21), the OES measurements show a good agreement with the Cruden model, as previously shown for the radiance profile in Figure 16, while the TDLAS measurements show a better agreement with the Park/Johnston model. This discrepancy may be attributed to a boundary layer biasing the LAS number density measurement low. Analysis was performed to incorporate the effect of the boundary layer in the measurement, as discussed in Ref. [9], which appears to reconcile the measurements at some conditions. However, a 5 – 10% gap persists between the measurements at a number of conditions, suggesting the boundary layer may not be fully accounted for. Note that the  $\text{CO}_2$  number density is more impacted than temperature by shock deceleration in the reacting flow. This causes the radiation profile in Fig. 16 to be largely unimpacted by deceleration even though the post-shock condition is affected. For the frozen cases, the TDLAS measurements are again slightly under the temperature profiles obtained from OES. This discrepancy is largely within the uncertainty of the two measurement techniques as LAS estimates a 4.1 - 6.6% uncertainty as shock velocity increases from 2 – 3 km/s and OES estimates the fitting uncertainty as 2%. The LASTA temperatures generally lie between the temperatures obtained with both methods. Other sources of discrepancy could include the possibility of a turbulent boundary layer resulting in a thicker cool gas region than is accounted for in the analysis or the possibility that a complex thermal non-equilibrium persists between the asymmetric stretch mode and the rotational energy mode of the gas. The OES temperature will be primarily sensitive to the asymmetric stretch temperature, while the LAS temperature is purely a rotational temperature in these data. For more details about the LAS uncertainties, refer to the companion paper [9]. For all cases, the number density profiles measured by both LAS and OES are within the uncertainties of the measurements and agree with LASTA within the uncertainty. In the future, an updated line selection can be utilized in the LAS technique to reduce uncertainty and an experimental investigation of the boundary layer can be conducted. Lastly, in the future the TDLAS measurements will be used to produce a simulated radiance profile that can be compared directly to the emission measurements.

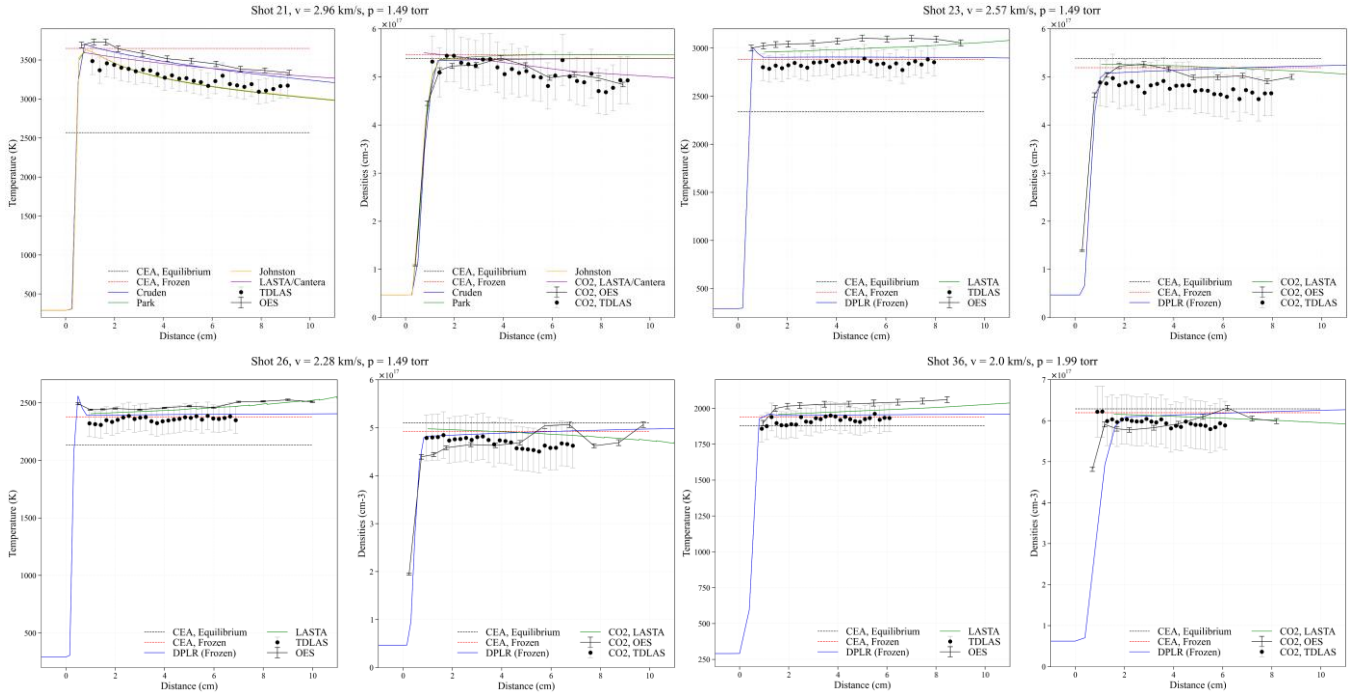


Figure 17: Comparison between temperature and CO<sub>2</sub> number density profiles measured by OES and TDLAS and predicted by CFD and LASTA simulations.

## VII. Conclusions

A test series was performed in the EAST facility aiming to reconstruct the backshell radiation measured by the MEDLI2 sensors during the Mars2020 entry. OES measurements were performed and compared to CFD simulations using three different kinetic models, referred as Park, Johnston and Cruden. The Park and Johnston models gave similar results for most cases, while the Cruden model tends to predict slower chemistry than the other two. The chemistry appeared to be frozen below 2.7 km/s for all models and in the experiment. At higher velocity, the measured radiance lay between the different models, with the Park and Johnston models underpredicting the radiation by about 10%, while the Cruden model overpredicted it by up to 7%, but giving better agreement in many cases. These observations appear true while looking at both the radiance immediately following and 300  $\mu$ s behind the shock front.

For backshell radiation, particularly at the radiometer location, most of the gas emitting the radiation impacting the backshell will have to travel more than 1 and 3 ms from the shock front at the test conditions of 1.1 and 1.5 Torr, respectively. At 1.1 Torr, taking into account the relaxation time to equilibrium, the prediction is expected to be to between 3 - 6.5% low (Park/Johnston) or 2% high (Cruden) at the heat flux gauge locations. At 1.5 Torr, most of the radiation is expected to come from shock velocity between 2.1 to 2.6 km/s which were found to be frozen in the timescale of the experiment, and uncertainty on the real flight measurement could not be determined.

The measured radiance in the frozen cases was consistently found to be higher than the frozen radiance predicted by CEA. This discrepancy was explained by shock deceleration effects that were simulated with the LASTA code. The LASTA simulations were able to reconcile differences up to 15% in cases where chemistry is expected to be frozen, and good agreement between measurements and frozen radiance predicted by LASTA were found for all shots below 2.7 km/s. This paper showed the importance of taking

into account the shock velocity history while comparing predictions and simulations and should be part of systematic analysis in the future.

Comparison with simultaneous LAS measurements were also performed. Temperatures inferred from OES were found to be close to the temperature measured by LAS but consistently higher, with up to 10% discrepancy. Boundary layer absorption was taken into account and reconcile the two techniques in some cases, but discrepancy was still observed, suggesting that this effect is not fully taken into account. A better uncertainty analysis on the OES temperature measurement should also be performed in the future for such comparison. On the other hand, CO<sub>2</sub> number density profiles measured by both techniques showed a good agreement for all cases studied. In the future, comparison of the radiance inferred from LAS data and OES measurements will be performed.

## References

- [1] C. Y. Tang, D. K. Prabhu, H. Alpert and B. A. Cruden, "MEDLI2: MISP Inferred Aerothermal Environment and Flow Transition Assessment," *AIAA SCITECH 2022 Forum*, no. AIAA 2022-0552, 2022.
- [2] T. R. White, M. Mahzari, M. A. Ruth, C. Y. Tang, C. D. Karlgaard, H. Alpert, H. S. Wright and C. Kuhl, "Mars Entry Instrumentation Flight Data and Mars 2020 Entry Environments," *AIAA SCITECH 2022 Forum*, no. AIAA 2022-0011, 2022.
- [3] B. A. Cruden, A. M. Brandis and D. K. Prabhu, "Measurement and Characterization of Mid-wave Infrared Radiation in CO<sub>2</sub> Shocks," *11th AIAA/ASME Joint Thermophysics and Heat Transfer Conference*, Vols. AIAA 2014-2962, 2014.
- [4] C. O. Johnston and B. Kleb, "Uncertainty Analysis of Air Radiation for Lunar-Return Shock Layers," *Journal of Spacecraft and Rockets*, vol. 49, no. 3, pp. 425-434, 2012.
- [5] R. A. Miller, C. Y. Tang, T. R. White and B. A. Cruden, "MEDLI2: MISP Measured Aftbody Aerothermal Environments," *AIAA SCITECH 2022 Forum*, no. AIAA 2022-0551, 2022.
- [6] A. M. Brandis, T. R. White, D. Sanders and J. Hill, "Simulation of the Schiaparelli Entry and Comparison to Aerothermal Flight Data," *AIAA Aviation 2019 Forum*, no. AIAA 2019-3260, 2019.
- [7] B. A. Cruden, A. M. Brandis, T. R. White, M. Mahzari and D. Bose, "Radiative Heating During Mars Science Laboratory Entry: Simulation, Ground Test, and Flight," *Journal of Thermophysics and Heat Transfer*, vol. 30, no. 3, pp. 642-650, 2016.
- [8] C. O. Johnston, "Evaluating Shock-Tube Informed Biases for Shock-Layer Radiative Heating Simulations," *Journal of Thermophysics and Heat Transfer*, vol. 35, no. 2, pp. 349-361, 2020.
- [9] C. Jelloian, N. Minesi, R. M. Spearrin, A. Tibere-Inglesse, M. E. McDonald and B. A. Cruden, "Examination of Mars2020 shock-layer conditions via infrared laser absorption spectroscopy of CO<sub>2</sub> and CO," *2023 AIAA SciTech forum, National Harbor, MD*, 2023.
- [10] B. Cruden, R. Martinez, J. Grinstead and J. Olejniczak, "Simultaneous Vacuum-Ultraviolet Through Near-IR Absolute Radiation Measurement with Spatiotemporal Resolution in An Electric Arc Shock Tube," *41st AIAA Thermophysics Conference*, Vols. AIAA 2009-4240, AIAA, San Antonio, TX, 2009.
- [11] S. P. Sharma and C. Park, "Operating Characteristics of a 60- and 10-cm Electric Arc-Driven Shock Tube-Part 11: The Driven Section," *Journal of Thermophysics and Heat Transfer*, vol. 4, no. 3, pp. 266-272, 1990.
- [12] E. Whiting, C. Park, L. Yen, J. Arnold and J. Paterson, "NEQAIR96, Nonequilibrium and Equilibrium Radiative Transport and Spectra Program: User's Manual," Technical Report NASA RP-1389, Ames Research Center, Moffett Field, 1996.
- [13] S. Gordon and B. McBride, "Computer program for calculation of complex chemical equilibrium compositions and applications. Part 1: Analysis," NASA RP-1311, 1994.
- [14] B. J. McBride and S. Gordon, "Computer Program for Calculation of Complex Chemical Equilibrium Compositions and Applications II. User's Manual and Program Description," *NASA RP-1311-P2*, June 1996.

- [15] A. M. Brandis, C. O. Johnston, B. A. Cruden and D. K. Prabhu, "Investigation of Nonequilibrium Radiation for Mars Entry," *51st AIAA Aerospace Sciences Meeting including the New Horizons Forum and Aerospace Exposition, Aerospace Sciences Meetings*, no. AIAA 2013-1055, 2013.
- [16] B. A. Cruden and A. M. Brandis, "Measurement and Prediction of Radiative Non-equilibrium for Air Shocks Between 7-9 km/s," *American Institute of Aeronautics and Astronautics*, no. AIAA 2017-4535, 2017.
- [17] M. J. Wright and D. Bose, "Data-Parallel Line Relaxation Method for the Navier-Stokes Equations," *AIAA Journal*, vol. 36, no. 9, pp. 1603-1609, 1998.
- [18] B. A. Cruden, A. M. Brandis and D. K. Prabhu, "Compositional Dependence of Radiance in CO<sub>2</sub>/N<sub>2</sub>/Ar Systems," *44th AIAA Thermophysics Conference*, no. AIAA 2013-2502, 2013.
- [19] C. Park, *Nonequilibrium hypersonic aerothermodynamics*, New York: Wiley, 1989.
- [20] J. W. Streicher, A. Krish and R. K. Hanson, "Coupled vibration-dissociation time-histories and rate measurements in shock-heated, nondilute O<sub>2</sub> and O<sub>2</sub>-Ar mixtures from 6000 to 14 000 K," *Physics of Fluids*, vol. 33, no. 5, p. 056107, 2021.
- [21] B. A. Cruden, A. M. Brandis and M. E. MacDonald, "Characterization of CO Thermochemistry in Incident Shockwaves," *AIAA AVIATION Forum, 2018 Joint Thermophysics and Heat Transfer Conference*, no. 2018-3768, 2018.
- [22] C. O. Johnston, "Shock-Layer Radiation Insights Available Through Flowfield-Property Binning," *AIAA SCITECH 2022 Forum*, no. 2022-2396, 2022.
- [23] A. M. Brandis, B. A. Cruden, D. Prabhu, D. Bose, M. McGilvray and R. Morgan, "Analysis of Air Radiation Measurements Obtained in the EAST and X2 Shocktube Facilities," *10th AIAA/ASME Joint Thermophysics and Heat Transfer Conference*, no. AIAA 2010-4510, 2010.
- [24] P. L. Collen, M. Satchell, L. Di Mare and M. McGilvray, "The influence of shock speed variation on radiation and thermochemistry experiments in shock tubes," *Journal of Fluid Mechanics*, vol. 948, p. A51, 2022.
- [25] M. Satchell, L. Di Mare and M. McGilvray, "Flow Nonuniformities Behind Accelerating and Decelerating Shock Waves in Shock Tubes," *AIAA Journal*, vol. 60, no. 3, pp. 1537-1548, 2021.
- [26] M. Satchell, M. McGilvray and L. Di Mare, "Analytical Method of Evaluating Nonuniformities in Shock Tube Flows: Theory and Development," *AIAA Journal*, vol. 20, no. 2, pp. 654-668, 2021.
- [27] P. L. Collen, M. Satchell, L. di Mare and M. McGilvray, "Analysis of Shock Deceleration Effects on Radiation Experiments in the NASA Electric Arc Shock Tube," *AIAA SCITECH 2022 Forum*, no. 2022-0267, 2022.
- [28] D. G. Goodwin, H. K. Moffat, I. Schoegl, R. L. Speth and B. Weber, "Cantera: An object-oriented software toolkit for chemical kinetics, thermodynamics, and transport processes," Version 2.6.0, 2022. [Online]. Available: <https://www.cantera.org>.
- [29] J. Clarke, M. McGilvray and L. Di Mare, "Numerical model for non-equilibrium shock tube flow," in *Radiation and High Temperature Gases Workshop*, 2022.
- [30] J. Clarke, M. McGilvray and L. Di Mare, "Numerical simulation of a shock tube in thermochemical non-equilibrium," in *AIAA SciTech conference*, 2023.
- [31] B. A. Cruden and A. M. Brandis, "Analysis of Shockwave Radiation Data in Nitrogen," *AIAA Aviation 2019 Forum*, no. AIAA 2019-3359, 2019.
- [32] A. C. Tibere-Inglesse and C. A. Brett, "Analysis of nonequilibrium atomic and molecular nitrogen radiation in pure N<sub>2</sub> shockwaves," *Journal of Quantitative Spectroscopy and Radiative Transfer*, vol. 290, p. 108302, 2022.